JMEPEG (2018) 27:2899–2909
https://doi.org/10.1007/s11665-018-3380-0

1059-9495/$19.00

Effect of Pore Size, Morphology and Orientation on the Bulk Stiffness of a Porous Ti35Nb4Sn Alloy

Carmen Torres-Sanchez, John McLaughlin, and Ross Bonallo

(Submitted November 18, 2017; in revised form February 24, 2018; published online April 30, 2018)

The metal foams of a titanium alloy were designed to study porosity as well as pore size and shape independently. These were manufactured using a powder metallurgy/space-holder technique that allowed a fine control of the pore size and morphology; and then characterized and tested against well-established models to predict a relationship between porosity, pore size and shape, and bulk stiffness. Among the typically used correlations, existing power-law models were found to be the best fit for the prediction of macropore morphology against compressive elastic moduli, outperforming other models such as exponential, polynomial or binomial. Other traditional models such as linear ones required of updated coefficients to become relevant to metal porous sintered macrostructures. The new coefficients reported in this study contribute toward a design tool that allows the tailoring of mechanical properties through porosity macrostructure. The results show that, for the same porosity range, pore shape and orientation have a significant effect on mechanical performance and that they can be predicted. Conversely, pore size has only a mild impact on bulk stiffness.

Keywords elastic modulus, hypothesis-driven manufacture, pore morphology, porosity, TiNbSn

1. Introduction

Tailoring mechanical properties, and in particular stiffness, through the introduction of engineered porosity in a matrix presents opportunities for the creation of multiphase and multifunctional materials. Considering one of the phases as void, or air, the exploitation of their structural, thermal, acoustic, filtration or wicking properties finds applications in a myriad of fields. For example, the stiffness-to-weight ratio can be optimized to match the mechanical properties of bone and these cavities may be engineered to promote cell regeneration and vascularization. This twofold role, along with a biocompatible material, ensures the successful long-term implantation of load-bearing orthopedic implants. This optimization also applies to lightweight composite materials used by the transport industry pursuing a greener approach. Automotive components made out of porous beams which perform on a par with their solid structural counterparts but weigh less will reduce fuel consumption and thereby generate lower CO_2/NO_x emissions. Therefore, a design and manufacturing strategy that allows engineering the macrostructure of the porous material and permits the tailoring of its mechanical properties to suit the application is a much sought-after tool.

An extensive body of work that relates mechanical properties to volumetric porosity in a porous solid has been reported in the literature, and well-established models have been reported over the years. There exists a general agreement that bulk porosity (or porosity fraction) is negatively correlated to stiffness and strength. This correlation has traditionally been classified into linear (Ref 1, 2), power (Ref 3-7), exponential (Ref 8-10) and other miscellaneous models (i.e., polynomial and binomial distributions) (Ref 11-15). These mathematical relationships have been used to characterize foams, soil and ceramics (Ref 16), and generally consider the voids as spheroids in a regular arrangement with no regard to their size or shape. The effect of pore morphology on mechanical properties has been less often investigated. Seminal works by Wu (Ref 17) and Bert (Ref 18) rely on power correlations in which pore shape and orientation are considered, but they are truly applicable only to low porosity ranges ($< 20\%$). Pore orientation and aspect ratio has been recently studied in porous rock (Ref 19). Ondracek and Boccaccini (Ref 20) developed a power regression in which aspect ratio can be considered, as well as orientation of pores with respect to loading direction. This relationship is most relevant in this study, since both aspect ratio and orientation are hypothesized to have an impact on mechanical properties of porous materials.

The shape and morphology of a cavity in a porous material can be created by the use of space holders that are deployed into the green body (e.g., by mixing them with raw powdered material and pressed together) and then carefully extracted (e.g., through gentle thermal processes that avoid internal stresses, striation or deformation of the pore struts) to leave behind a cavity that replicates the exact shape and size of the original space holder.

Ammonium hydrogen carbonate (Ref 21, 22), carbamide (Ref 23, 24), sodium fluoride (Ref 25), and chloride (Ref 26), saccharose (Ref 27), and PMMA (Ref 28), starches (Ref 29, 30) and Mg spacers (Ref 31) have been employed successfully as space holders. This technique is widely used along with powder metallurgy for the fabrication of engineered metal and ceramic foams porous solids. Powder metallurgy presents advantages such as ease of handling metal powders for fine control of volumetric porosity and lower-than-melting-point temperatures employed in the process, which is crucial when dealing with titanium foams due to their affinity with oxygen.

Carmen Torres-Sanchez, John McLaughlin, and **Ross Bonallo**, Wolfson School of Mechanical, Electrical and Manufacturing Engineering, Loughborough University, Loughborough, Leicestershire LE11 3TU, UK. Contact e-mail: c.torres@lboro.ac.uk.

This is a hypothesis-driven study on the effect that pore size and pore morphology have on the mechanical properties, in particular on stiffness, of a porous material. In this work, the matrix of the porous solid was a Ti-based alloy (TiNbSn) prepared via powder metallurgy and mechanical alloying, with a typical $\alpha' + \beta$-phase crystal structure with potential for shape memory and superelasticity through an appropriate thermomechanical treatment (Ref 32), resistant to corrosion (Ref 33), Ni-free and therefore non-toxic. The space holders employed for the careful creation of pores were carbamide particles and PET fibers, preferred for their removal solely via thermal treatment and without solvents. Firstly, the space holder volumetric content was varied for a study on the impact of porosity on stiffness. Then, it remained constant, while the pore size and shape were varied for an independent study on the effect of pore morphology. Characterization of mechanical, physical and porosimetry features supported mathematical correlations that were established to predict trends arising from porosity and pore morphology variations. Concurrently, the fitness of the porous materials models reported in literature was assessed when they were applied to the metal porous materials manufactured for this study.

2. Materials and Methods

2.1 Porous Specimens Preparation

Elemental powders of Ti (Alfa Aesar, USA, 99.5% purity, $\leq$ 45 μm, -325 mesh), Nb (Aldrich, GE, 99.8% purity, $<$ 45 μm, -325 mesh) and Sn (Alfa Aesar, USA, 99.8% purity, $\leq$ 45 μm, -325 mesh) were blended together according to the desired composition of Ti 61 wt.%, Nb 35 wt.% and Sn 4 wt.%. This alloy is referred as Ti35Nb4Sn hereafter. Mechanical alloying was performed in a planetary ball mill (Fritsch pulverisette 6 Monomill, GE) under inert (argon) atmosphere and using a stainless steel grinding jar and with 10 mm diameter stainless steel balls. The ball-to-powder weight ratio was 10:1. The milling was carried out at room temperature with a rotation speed of 200 rpm for 12 h. This preparation time was chosen in accordance with previous experimental work that focused on the influence of ball-milling time and the quality of the resulting mechanically alloyed powder material (Ref 34).

Stearic acid (CH_3 $(CH_2)_{16}$ COOH, 2 wt.%) was added as a lubricant, and its role was twofold: (i) to be absorbed on the surface of the metal particles and assist the development of a desired fine microstructure during ball milling; and (ii) to prevent cold welding to the surface of the jar and balls during milling. Previous studies have shown this wt.% to be a good compromised amount to promote alloying while preventing fracturing as the dominant effect (Ref 35).

The ball-milled powders were mixed with the space-holder materials: (i) carbamide ($CO(NH_2)_2$) crystals (Fisher, UK, 99% purity) in two particle size ranges: 180-300 μm and 300-500 μm, and (ii) PET (Lohmann & Rauscher Int, AUS) fibers, 167 μm in diameter and length in the range 350 μm-3.7 mm, rendering them high aspect ratio fibers. The powder-to-space-holder volume ratio used was adjusted to yield a certain nominal volumetric porosity ratio. In this way, the volumetric porosity, the pore size and the pore morphology could be controlled and studied independently. Samples of each volumetric porosity were prepared at least in quintuplicate. The powder/space-holder mixture was then uniaxially cold compacted at a pressure of 250 MPa for the particles and 300 MPa for the fibers into cylindrical green compacts with a diameter of 16 mm and a height of 8 mm. These were placed in a calcination oven, heated at 2 °C/min from room temperature up to 250 °C for the crystals and 500 °C for the fibers and kept at that temperature for 2 h to sublimate the space holders and leave voids behind. The subsequent sintering stage took place in an atmosphere-controlled (argon) furnace (Lenton Thermal Designs, UK) previously vacuum-flashed thoroughly. The green compacts, with only the metal powders forming the porous structure, were heated up to 1100 °C at a heating rate of 5 °C/min, and held at this temperature for 3 h. This stage consolidated both the macro- and microstructure. The furnace was then allowed to cool to room temperature. The samples were wet ground and polished using a 240-grit silicon carbide cloth. Finally, they were cleaned using acetone and soapy water in an ultrasonic bath for 5 min and then left to be air dried.

2.2 Characterization of the Alloy Powders and Sintered Porous Specimens

Phase constituents in the ball-milled powders and sintered porous scaffolds were characterized using x-ray diffractometry (AXS D8 Advance glancing, Bruker, UK) with 1.5046 nm wavelength Copper K alpha radiation source. An organic contamination analysis was performed on the ball-milled and sintered powder to ascertain the presence of contaminants. The specimen's surface was examined with a scanning electron microscope (Quanta 3D FEG dual beam, 3.5 nm, 30 kV, FEI, USA). A microCT (X-Tek CT bench-top, USA) system equipped with a 160 keV x-ray source and a 12-bit CCD camera was used for internal inspection of the sintered specimens. The samples were scanned at $>$ 6 μm resolution. VGStudio Max software was used for volumetric reconstruction and bulk analysis.

Scamp v1.1 was utilized to assess sphericity and quantify void features in the sintered microstructure by 'inflating' spheres or oblates in integer multiples until solid was encountered. Mercury porosimetry was performed using an Autopore-IV porosimeter (Micromeritics Instrument Corp, USA) to determine mercury injection porosity, pore throat size distribution and generate air/mercury drainage phase capillary pressure curves. Mercury was injected into the sample at incremental pressure steps from 1.5 to 30.0 psia using nitrogen gas as the displacing medium until equilibrium (i.e., the rate of intrusion drops below 0.001 μL/g-s), and then from 30 to 60,000 psia, using hydraulic oil as the displacing medium. Mercury saturation and capillary pressure were used to calculate bulk porosity and open porosity fractions of the specimens.

2.3 Mechanical Testing

The compression experiments were conducted at room temperature on a 3367 universal testing machine (Instron, UK) with a 30-kN load cell. Each sample was loaded and unloaded at a constant speed of 1 mm/min between a minimum strain of 0% and a strain value which increased in 0.1% steps over consecutive 7 loops to a ε_{max} 0.7%. Finally, the scaffolds were tested at a compressive rate of 1 mm/min until collapse to determine their compressive stiffness (i.e., elastic moduli).

3. Results

The constituent elements, the powder after ball milling and also after sintering were tested to identify the components in the alloy (Fig. 1). It can be observed in Fig. 1(d) that the stearic acid additive was completely removed from the mixing powders by the end of the ball-milling process, so there was no organic contamination present in the powders. This was confirmed with a further contamination analysis. Organic contamination content (i.e., C, N, H) was investigated. The results showed virtually no contamination (0 %C ± 0.1% error, 0 %H ± 0.1% error, 0 %N ± 0.3% error) in all the samples. As expected, the sintered alloy exhibited an α′+β-phase crystal structure, with β crystals stabilized at room temperature which contributes to a lowering in stiffness when compared to Ti-only structures.

SEM images were used for pore size measurements (Fig. 2). Samples fabricated with particles in the range 180-300 μm presented pores of average values of 257.44 μm by 356.24 μm (standard deviation 71.84 and 93.99, respectively), and those in the range 300-500 μm, 348.39 μm by 489.78 μm (standard deviation 106.71 and 148.52, respectively).

Samples fabricated using the high aspect ratio fibers in the range 350 μm-3.7 mm and thickness 167 μm presented pores of average length value 1.545 mm (standard deviation 0.651 mm) and average thickness 167.336 μm (standard deviation 15.937 μm).

Bulk porosity (i.e., total porosity, which includes the intrinsic porosity due to the compaction of the powders, as well as the closed porosity) and open porosity measurements obtained from Mercury porosimetry tests (Fig. 3) are presented in Table 1.

The moduli of elasticity in compression, E^*, obtained from the mechanical tests were compiled along with the experimental values of density and apparent porosity (vol.%) in terms of mean values considering all specimens (Table 2). Apparent porosity was calculated by the ratio between the measured density of the porous scaffold and the density of the sintered sample with no porosity incurred by the inclusion of pore agents. These results were confirmed via microCT studies and volumetric reconstructions (Fig. 4)

The increasing strain versus stress relationships for the particle-void 300-500 μm and the fiber-void were selected for direct comparison (Fig. 5) because these two sets share a similar void-volume value along a plane. The results show a high elasticity for the samples with low nominal porosity and low residual strain at the end of the each cycle. As volumetric porosity increases, the maximum compressive stresses attained are reduced for a same value of strain. When the fiber was used as a porogen agent, the specimens exhibited more hysteresis and less elasticity than their particle-void counterparts.

The stiffness ratio, i.e., elastic modulus of the porous sample (E^*) to that of the solid sintered sample (E_s), and the ratio of the porous sample density (ρ^*) to that of the solid sintered sample (ρ_s), was calculated. Porosity fraction (P) was reported as $[1-(\rho^*/\rho_s)]$. Stiffness ratio and porosity fraction were plotted (Fig. 6). Overlaid onto them are typical regression models reported in the literature and currently used to predict the relationship between volumetric porosity and compression elastic moduli in porous materials. The numerical results are compiled in Table 3 which shows results considering porosity fraction independently from pore size and pore morphology. Each of the models that have been consolidated in literature over the years can be classified as linear, power, exponential and other author's models that use polynomial or binomial correlations.

The original models were plotted along the datasets under study in this work (Fig. 6) to establish whether those current relationships were applicable to the present study.

Furthermore, the datasets were interrogated in order to obtain more updated model coefficients that were more suitable for the actual microstructure of the alloy. These new

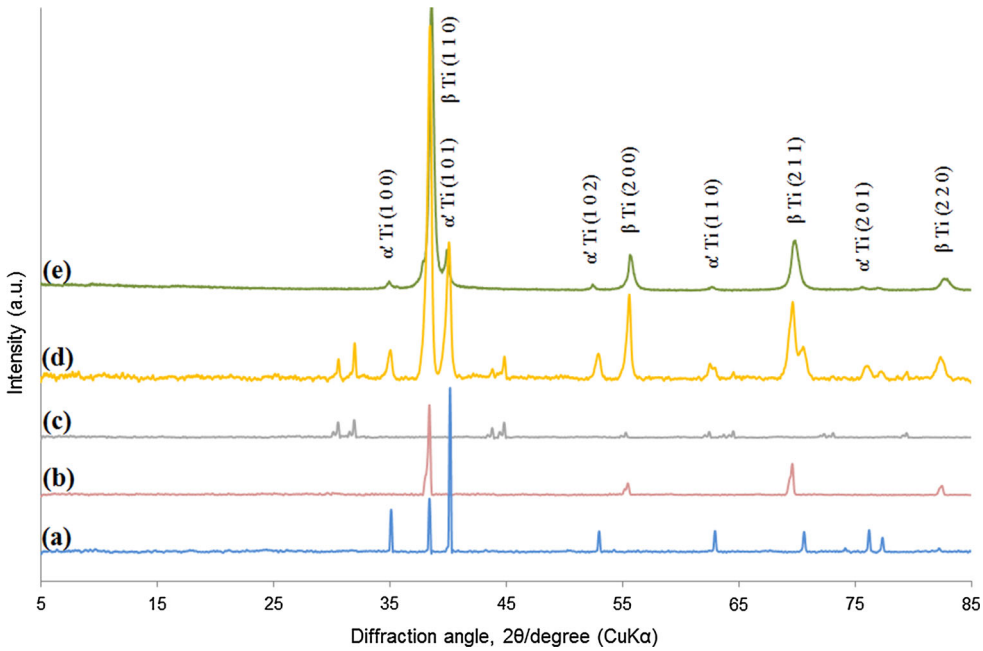

Fig. 1 XRD patterns acquired from: constituent elements (a) Ti, (b) Nb and (c) Sn, (d) mixed powders after ball milling for 12 h; (e) after sintering at 1100 °C for 3 h

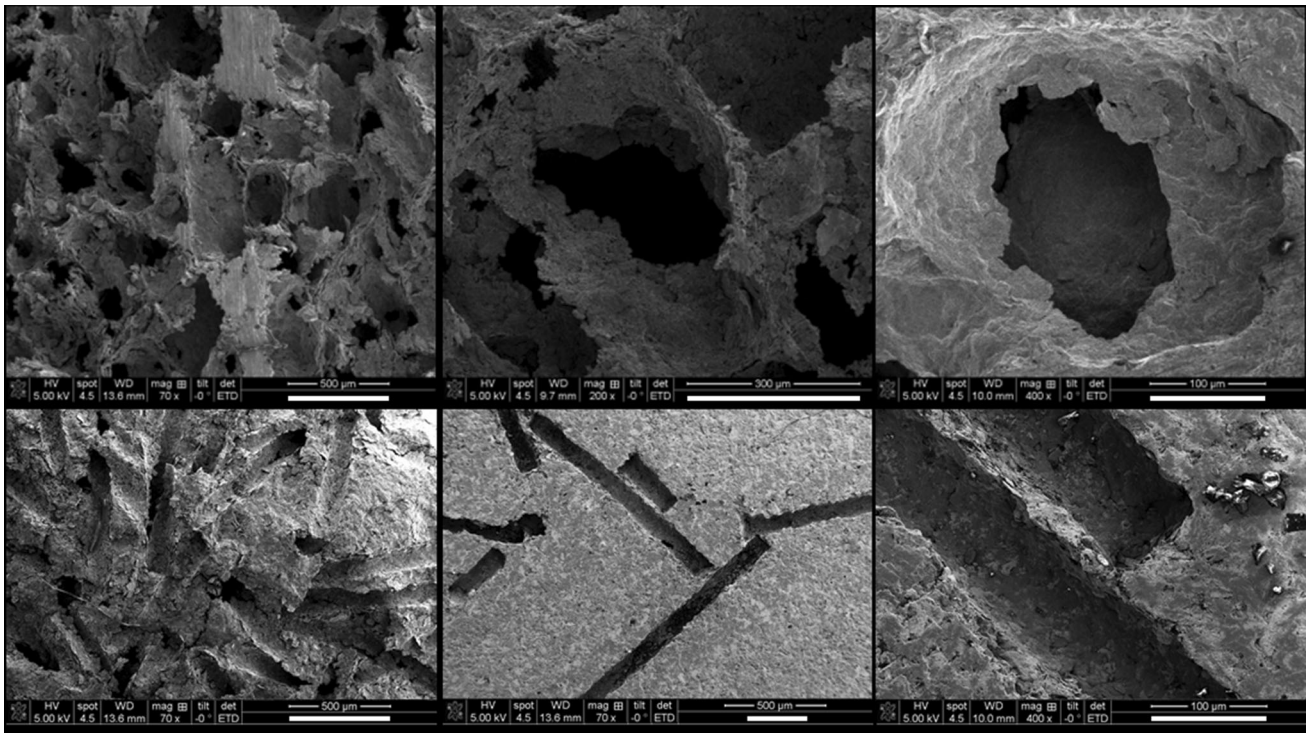

Fig. 2 SEM images of scaffold surfaces and pores for specimens fabricated using a particle porogen (top row) and a fiber porogen (bottom row). Scale bars: 500 μm (1st column), 300 μm (middle column), 100 μm (last column)

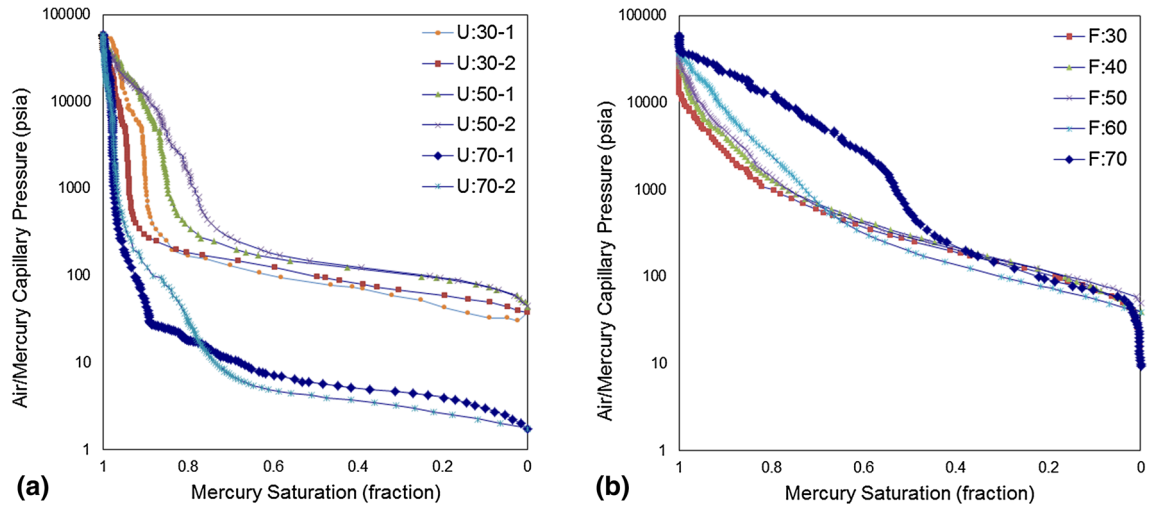

Fig. 3 Mercury saturation and capillary pressure for volumetric porosities 30-70% when the porogen agent is: (a) particle (U), 1: 180-300 μm, 2: 300-500 μm ranges, (b) fiber (F)

coefficients are presented along with the corresponding coefficient of determination, R^2 values (Table 3, last two columns).

In order to study the impact of pore morphology on mechanical stiffness, a power-extended correlation was identified and employed (Ref 20). Table 4 presents the results from the predictions that this model offers. In view of these results, further investigations were carried out to confirm aspects of sphericity, pore elongation and orientation (with respect to the compression plane) using 3D volumetric reconstructions of the porous specimens, in particular those of the fiber-porogen samples (F) (Fig. 8).

An iterative sum of squared errors optimization method was used to calculate the mean aspect ratio (i.e., z/x) and mean pore orientation factor for particles (i.e., $\cos^2 x_D$) in the two ranges for particle size (180-300 μm and 300-500 μm) based on the experimental pore size values (Fig. 2) and fiber length 350 μm-3.7 mm, and from 0° (i.e., perpendicularly loaded to the direction of the fibers) to 90° (i.e., parallel orientation) for the fiber. Table 4 presents the prediction of pore aspect ratio (z/x) and the orientation angle (x_D) based on the stiffness in the porous specimens (U and F) and have to be studied in tandem with the row of the corresponding power-law model in Table 3.

Table 1 Mercury porosimetry impregnation averaged results

Pore agent	Pore agent size	Nominal porosity, vol.%	Bulk porosity, vol.%	Open porosity, vol.%
Particle (U)	180-300 μm	30	40.5	16.3
		50	45.9	11.9
		70	78.3	62.4
	300-500 μm	30	32.6	18.1
		50	44.3	13.9
		70	61.7	60.2
Fiber (F)	167 μm	30	42.5	11.8
		40	47.1	12.8
		50	50.8	14.7
		60	61.9	15.1
		70	62.2	13.6

Table 2 Physical (i.e., porosity) and mechanical characterization results from designed specimens with a controlled porosity, pore size and pore shape

Pore agent	Pore agent size	Nominal porosity, vol.%	ρ^*, g/cm^3 (SD)	Apparent porosity, % (SD)	E^*, MPa (SD)
Particle (U)	180-300 μm	30	3.281 (0.084)	20.983 (0.349)	8629.867 (978.642)
		40	2.791 (0.092)	32.796 (0.382)	6138.133 (1067.032)
		50	2.531 (0.127)	39.050 (0.527) †(39.9)	6277.367 (610.434)
		60	2.056 (0.125)	50.486 (0.519)	4108.767 (1116.521)
		70	1.845 (0.126)	55.572 (0.523)	2399.200 (297.110)
	300-500 μm	30	3.269 (0.248)	21.285 (1.030) †(23.5)	9300.867 (934.911)
		40	2.972 (0.093)	28.422 (0.386)	6721.067 (476.724)
		50	2.499 (0.102)	39.816 (0.424) †(39.4)	5960.933 (802.822)
		60	2.101 (0.245)	49.399 (1.017)	5139.633 (741.133)
		70	1.740 (0.128)	58.056 (0.531) †(58.5)	2796.133 (1161.931)
Fiber (F)	167 μm	10	3.456 (0.597)	16.769 (2.479) †(13.6)	10599.608 (1023.623)
		20	3.145 (0.459)	24.254 (1.907)	7787.051 (292.376)
		30	2.897 (0.337)	30.222 (1.399) †(30.1)	7219.625 (2043.430)
		40	2.525 (0.172)	39.198 (0.712)	3965.524 (1976.912)
		50	2.201 (0.046)	46.998 (0.189) †(46.0)	3101.870 (679.977)

†Confirmed with microCT results. Result in brackets

Results from the 3D reconstructions yielded a z/x aspect ratio close to 10 and 83% of the fibers laying perpendicular to the compression direction (Fig. 7). Elongation of the fiber-voids was extracted and color coded for easy visualization, and orientation angles with respect to the plane can easily be seen on the top, side and front views in Fig. 7.

4. Discussion

The effect of bulk porosity on stiffness of a porous material has been widely studied and reported without considering the morphological features of the cavities. However, in this study we hypothesized that, in addition to porosity, size and aspect ratio can play an important role in the mechanical performance of a porous solid, and therefore, these have to be considered in order to predict accurately the properties of the material. Creating an α′+β-phase crystal structure in the alloy, like the one obtained in this study, already has an impact on the tailoring of the elastic modulus since the presence of β-phase modified the Young's moduli of the bulk material (Ref 32). This was achieved via powder metallurgy, an accessible technology that avoids harsh production environments. The use of space holders permitted the creation of voids that faithfully replicated the shape and geometry of the space holder itself, with no plastic deformation during consolidation and little pore shrinkage during sintering. These have a further effect on the bespoke realization of the controlled stiffness in the microstructure. The pore geometries obtained were very similar to the geometries of the space holder particles used, as per the SEM results. The open porosity measured by infiltration tests (Table 1) results in very low values, below 70% nominal porosity, when particles were used as pore agents, which demonstrates the pores are not interconnected. The value increases largely with a nominal porosity of 70%, when the structure reaches a tortuosity level sufficient to permit flow. This effect is depicted in Fig. 3(a), with the different mercury saturation fraction evolution pace when the air/mercury capillary pressure was increased. Conversely, the fiber-void samples never reached such values of interconnection despite large porosity values achieved (Fig. 3b). This result already indicates the microstructure and preference in pore orientation within those specimens.

The values obtained for the compressive elastic moduli were positively correlated to the density (Table 2). Specimens manufactured with particles (U) used as a porogen agent yielded elastic moduli values in the range (2.4-9.3 GPa), more specifically (2.4-8.6 GPa) for the smaller pore sizes and (2.8-9.3 GPa) for the large sizes. When fibers were used as a space holder (F), and in a similar range of densities, the range was

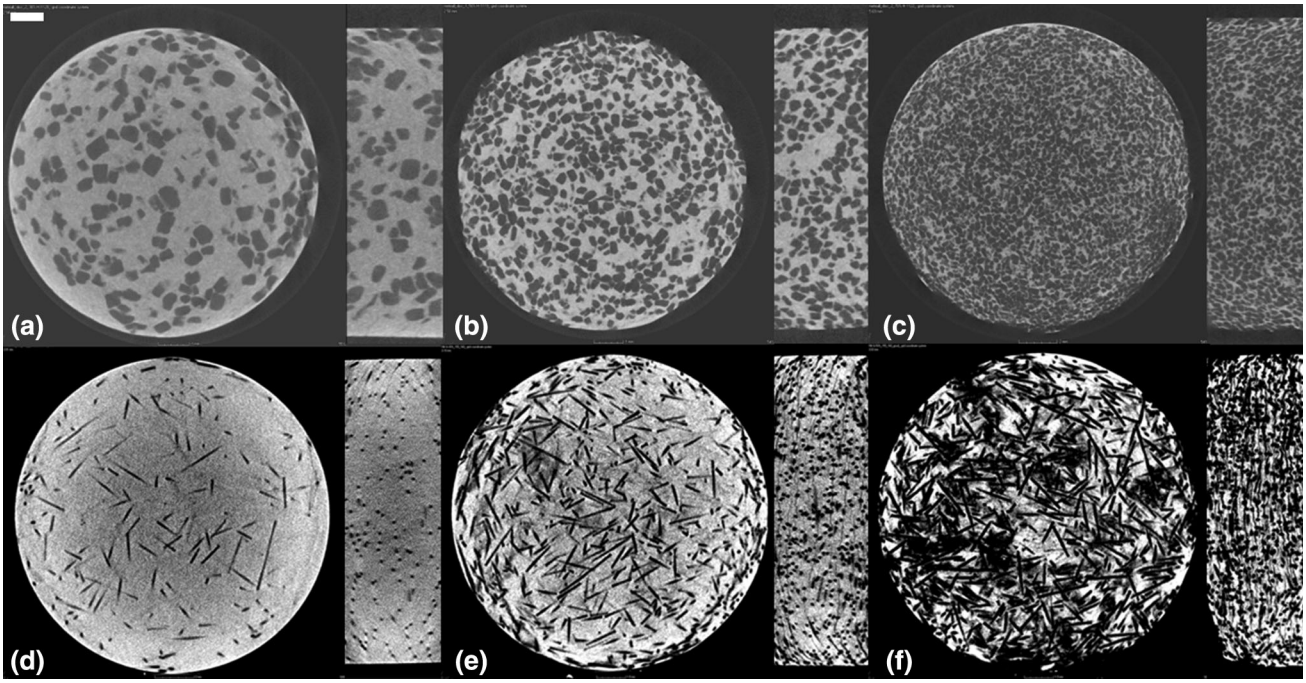

Fig. 4 MicroCT slices (xz and xy planes) of specimens manufactured with (a-c) particle porogen: nominal porosity 30% with pore range 300-500 μm, 50% with pore range 180-300 μm and 70% with pore range 180-300 μm and with (d-f) fiber porogen: nominal porosity 10, 30, 50%. Scale bar 1 mm

(3.1-10.6 GPa). For the sake of clarity, it should be noted that nominal volumetric porosity in fiber-void specimens had to be adjusted [i.e., reduced, starting at 10% instead of 30%] to achieve a similar porosity range to that exhibited by the particle-void specimens and therefore make the two sets comparable (Table 2). These values are in agreement with others reported in the literature for Ti-based alloys prepared via powder metallurgy/space-holder method regardless of the pore morphology (Ref 24, 30, 42, 43). Therefore, the influence of macropore size on the bulk mechanical stiffness of specimens in the same range of porosity was shown to be negligible.

Studies on the mechanical response to cyclic loading were conducted to 0.7% strain through an increasing regime. Specimens of nominal porosity 30, 40 and 50% and with an equivalent void-volume porosity along the plane showed good performance, and, as expected, the maximum stress incurred was negatively correlated with volumetric porosity.

Hysteresis increased and residual strain accumulated with an increasing volumetric porosity value (Fig. 5). Specimens manufactured with fibers as porogen agents presented a more significant accumulated residual strain than their particle-void counterparts for the same nominal porosity, which is indicative of failure by microfracturing (Fig. 5d, e, f). This result is in agreement with other studies (Ref 19, 44) in which specimens containing prolate pores subjected to a load transversal to the pore orientation exhibited compressive elastic moduli and strength much lower than those with parallel loads and/or pore aspect ratio close to unity.

In an attempt to assess whether the current reported models for the prediction of mechanical properties (in particular stiffness) with respect to porosity fraction in porous materials were suitable for metal alloy porous specimens, the datasets obtained in this study were overlaid directly onto the models and subsequently interrogated to optimize the fitting. As shown in Fig. 6a, linear models of the format $E^*/E_s = 1 - aP$, with the coefficients reported in the literature [i.e., constant a equals to 1 (Ref 1), 2 (Ref 2, 21, 36) or 2.6 (Ref 37)] do not offer a good fitting for the microstructures generated by the sintered powder alloy under study. Instead, the coefficients for a being 1.350, 1.252 and 1.612 for the particles in the ranges 180-300 μm, 300-500 μm and the fibers, respectively, yielded a more apt correlation. With regard to power regressions (e.g., $E^*/E_s = 1 - jP)^i$, using $j = 1$ as in Ref 3, the reported values that can be found in the literature correspond to ($i \sim 2$) for predominantly open cell foams (Ref 5) and spherical pores (Ref 4).

The overlays for the particle (U) results in this study are well-matched to those because the results yielded correlation values for exponent i equal to 1.954 and 1.714 for the particles 180-300 μm and 300-500 μm, respectively. On a similar trend, the overlays for the fiber porogen (F) results were agreeable with the typical power-law models and the regression result was 3.473. Similar values for i have also been found when the structure was predominantly open celled, loaded transversally to orientation of the voids [$i = 3$ (Ref 5)], and between 3 and 4 with increasing values of aspect ratio of randomly oriented oblate spheroids, as it is the case in the fiber-void samples. This value was found to be in the range 2.02-5.48 for pressed and sintered powders with a negative correlation between tortuosity in the material and the i value (i.e., a wider distribution of channels presents less tortuosity and therefore will render larger values for i) (Ref 38). More recent studies have found that experimental data can be fitted to a range for i from 2 to 4 based on the choice of porogen precursor (Ref 45). Therefore, it can be concluded that this power model is appropriate to predict the behavior of the microstructure created in the metal powder via powder metallurgy and space-holder sintering. Other power correlations, e.g., $E^*/E_s = 1 - uP^{2/3}$, were considered, and the overlays showed a certain degree of consistency with the

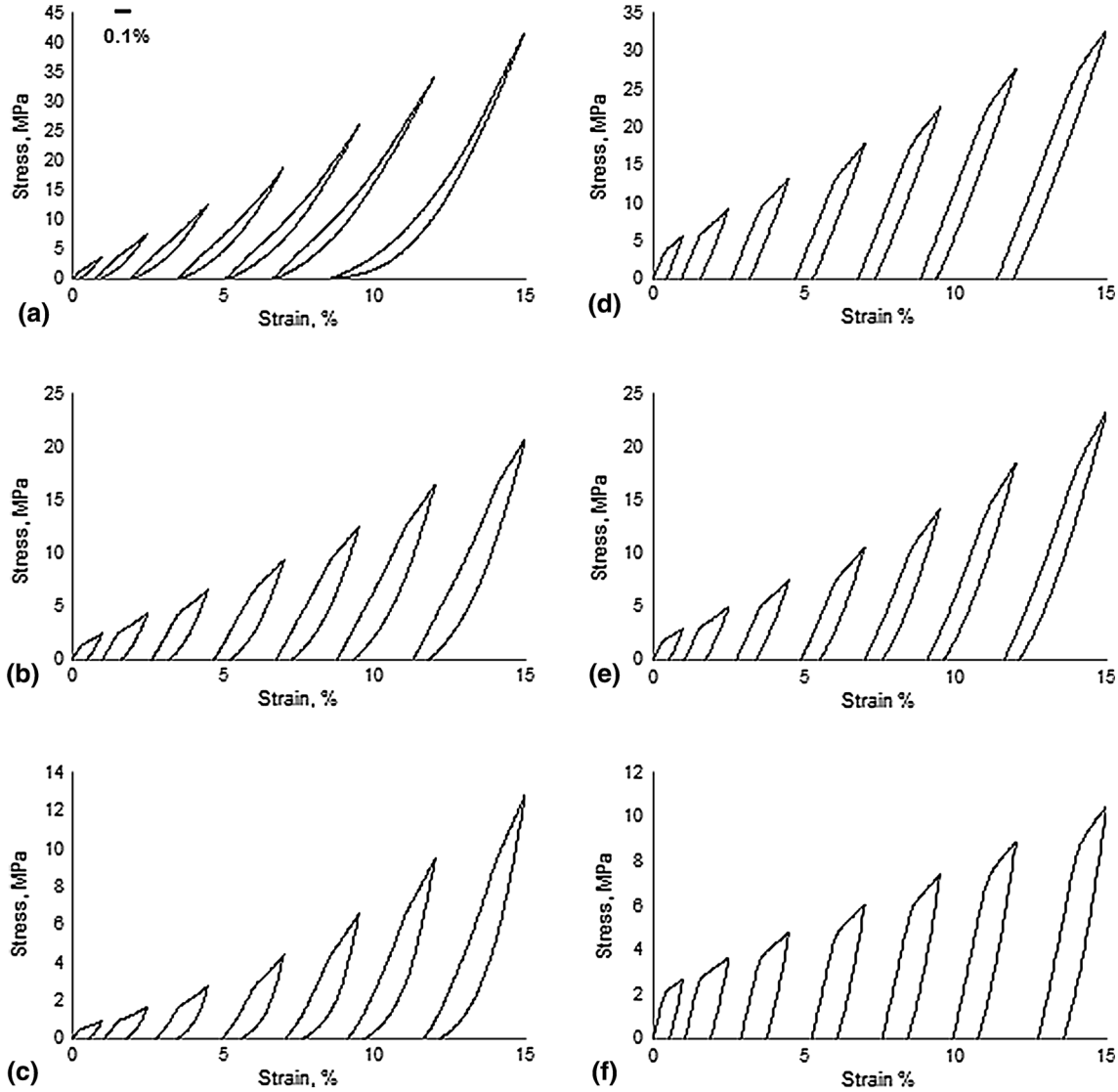

Fig. 5 Increasing strain cycles at 0.1% step-intervals: nominal 30-50% porosity (a, b, c) particle range 300-500 μm and (d, e, f) fiber 167 μm

models that exist for porous materials. The fitting value for u in this study was 0.989 for the particles (in particular 1.024 for the lower range 180-300 μm and 0.954 for the upper size range 300-500 μm). This result is in agreement with others reported in literature [$u = 1$ for cubic packing (Ref 7)]. Moreover, the fitting value for the fiber-voids was 1.123, when other values such as 1.15 for cubic packing of spherical pores (Ref 46), 1.21 for sintered alloys (Ref 6) and 1.3 in cast porous alumina (Ref 39) have been reported. Although with weaker R^2 values than those of the previous power model, this one is also suitable for the prediction of metal alloy sintered materials with space-holder-aided porosity. On the contrary, exponential regressions (i.e., $E^*/E_s = \exp(-\mathrm{m.P})$) were less suitable and the current models ill-fitting to the datasets from this study. They yielded values for the constant m of 2.036 and 1.833 for the particles in the smaller range and large range, respectively. The fiber-void set returned a value of 2.282. These fall only loosely between the upper and lower limits reported (2.7-4.3) by (Ref 8).The extended equation for the exponential dependence (i.e., $E^*/E_s = 1 - \exp(-r(1-\mathrm{P}))$, by (Ref 10), with $r = 0.5$) was only applicable for porosities around 50%, as shown in Fig. 6(c). Other correlations (Fig. 6d) present some degree of fitting, in particular models for inclusions of cubic shape by Paul (Ref 11) for the particles, models for effective Poisson's ratio and porosity-dependant factors of randomly distributed spherical pores (Ref 40) and metal-foam-derived relationships (Mondal et al.) (Ref 13).

Poor quality fitting was found with models reported by Spinner et al. (varying d and g) in Ref 14, which underestimate the compression elastic moduli ratio, and for Hashin's (Ref 41) (with a Poisson's ratio for the alloy of 0.3), which overestimates them. Because it is not explicitly described in Ref 41, it is hypothesized that Hashin et al's model refers to non-uniformly distributed isolated pores surrounded by a spherical shell of material (Ref 15), unlike the porous systems under study here, explaining in this way the poor suitability of the model for predicting the metal sintered porous macrostructure.

In light of these results, it is appropriate to conclude that typically reported power correlations are the ones that fit experimental data best for both the particle-void specimens, aligning to models describing open celled-spheroid inclusions, and the fiber-void ones, which follow the relationship of an

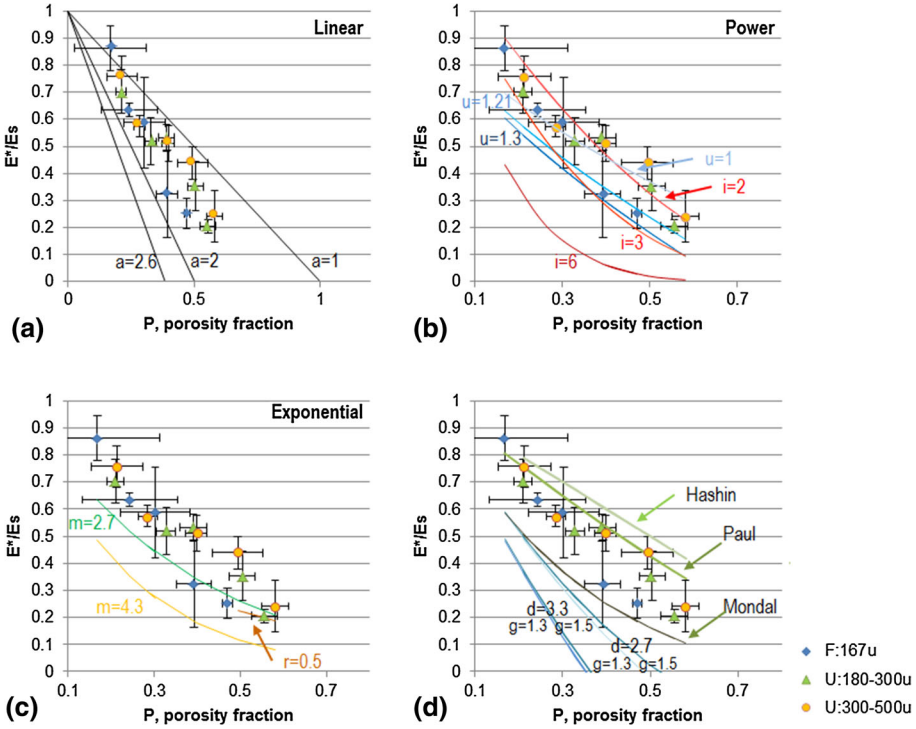

Fig. 6 Stiffness ratio vs. porosity fraction plotted against (a) linear, (b) power, (c) exponential and (d) other regressions. Blue diamonds for fiber-voids, green triangles for particle-void size range 180-300 μm and orange circles for size range 300-500 μm

Table 3 Compilation of comparison against established models for the prediction of stiffness using porosity and the results from the regressions study arising from this work

Model	Prediction by other authors	This work	R^2
Linear			
$E^*/E_s = 1 - aP$	a = 1 (Ref 1)	U: 180-300, a = 1.350	0.9415
	a = 2 (Ref 2, 36)	U: 300-500, a = 1.252	0.9298
	a = 2.6 (Ref 37)	F: 167, a = 1.612	0.8970
Power			
$E^*/E_s = (1 - jP)^i$	j = 1, i = 2 (Ref 4)	U: 180-300, j = 1, i = 1.954	0.9222
	j = 1, i = 2-3 (Ref 5)	U: 300-500, j = 1, i = 1.714	0.9248
	j = 1, i = 6 (Ref 38)	F: 167, j = 1, i = 3.473	0.9360
$E^*/E_s = 1 - uP^{2/3}$	u = 1 (Ref 7)	U: 180-300, u = 1.024	0.8542
	u = 1.21 (Ref 6)	U: 300-500, u = 0.954	0.8556
	u = 1.3 (Ref 39)	F: 167, u = 1.123	0.7399
$E^*/E_s = \left(1 - uP^{2/3}\right)^S$	S = 1.21 (Ref 20)	U: 180-300, S = 1.216	0.9084
		U: 180-300, S = 1.201	0.9161
		F: 167, S = 1.256	0.9742
Exponential			
$E^*/E_s = e^{-mP}$	m = 2.7-4.3 (Ref 8)	U: 180-300, m = 2.036	0.7783
		U: 300-500, m = 1.833	0.8191
		F: 167, m = 2.282	0.7969
$E^*/E_s = 1 - e^{-r(1-P)}$	r = 0.5 (Ref 10)	Only for porosities > 50%	
Other			
$E^*/E_s = \frac{(1-P^{2/3})}{(1-P^{2/3}+P)}$	Ref 11	See Fig. 6d	
$E^*/E_s = \frac{(1-P)^2}{(1+yP)}$	y = 1 (Ref 13)	See Fig. 6d	
	y = 1.1 (Ref 40)		
$E^*/E_s = \frac{1-P}{(1+wP)}$; $w = \frac{(1+\gamma_0)\cdot(13-15\gamma_0)}{2(7-5\gamma_0)}$; $\gamma_0 = 0.3$	Ref 41	See Fig. 6d	
$E^*/E_s = 1 - dP + gP^2$	d = 2.7-3.3	See Fig. 6d	
	g = 1.3-1.5 (Ref 14, 15)		

Table 4 The prediction of stiffness using pore morphology and orientation and the results arising from this work

Prediction model by Ref 20	This study		
$E^*/_{E_s} = (1 - P^{2/3})^S$; $S = 1.21 \cdot \left[\frac{z}{x}\right]^{1/3} \cdot \left[1 + \left(\left[\frac{z}{x}\right]^{-2} - 1\right) \cdot \cos^2 x_D\right]^{1/2}$	U: 180-300	$z/x \approx 1$	x_D = 10-90°
	U: 300-500	$z/x \approx 1$	x_D = 20-90°
	F: 167	z/x = 6-12	x_D = 20-30°

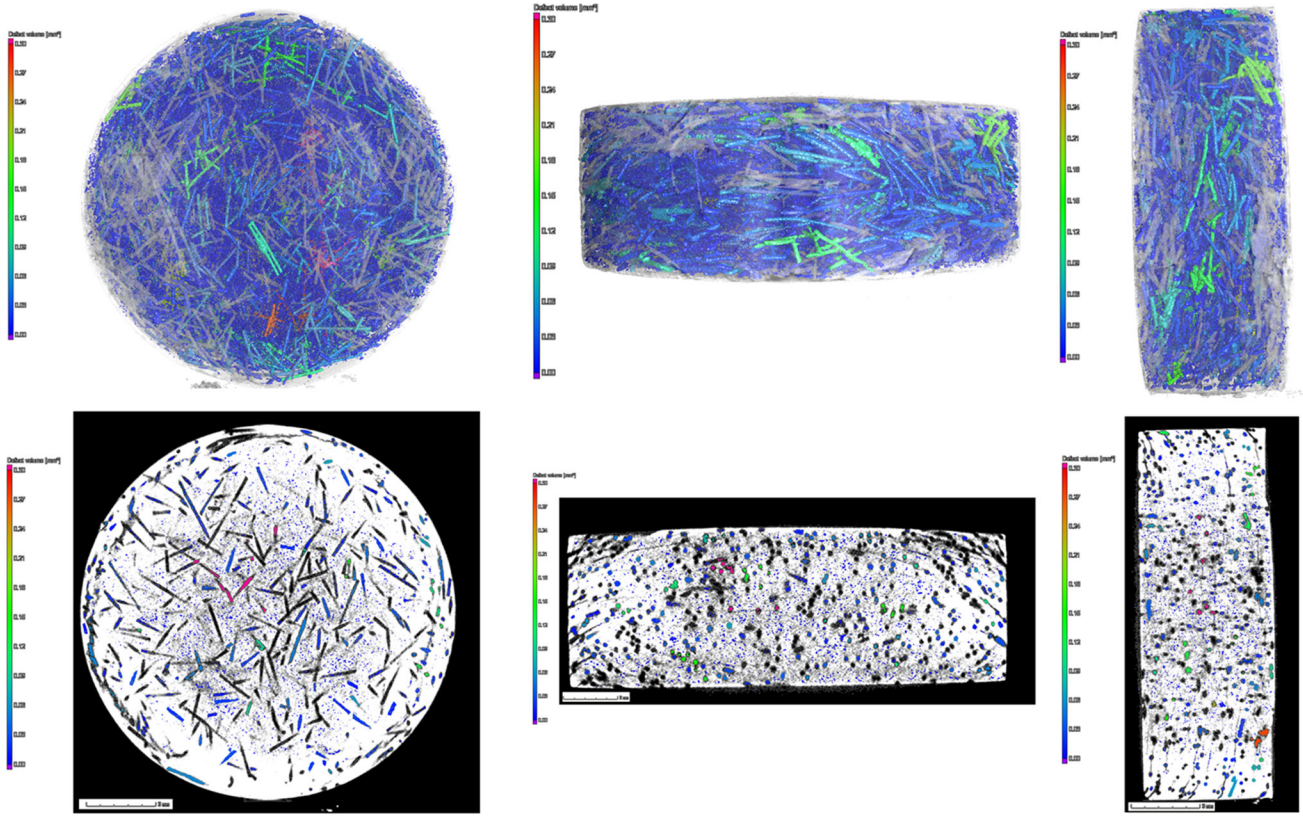

Fig. 7 MicroCT results from fiber-porogen sample (20% nominal porosity) showing top, side and front views. Scale bar: void volume

open-channeled pore loaded transversally. These results were confirmed with the outputs from mercury porosimetry test, which estimated the degree of open porosity in the samples, and microscopy and microCT slides, which allowed direct observations on the shape and orientation of the pores (Fig. 4). Linear models were also well suited provided new fitting coefficients were used instead of the existing reported ones that are limited to the special cases of very small sized non-interconnected spheres, typically created in ceramic matrices.

Those models mentioned have been proven very useful once again for the description of bulk stiffness of the microstructure. However, they do not inform about stiffness dependence on pore orientation or size. For this purpose, the power-law-based correlation reported in Ref 20 provided this study an extension to further consider the aspect ratio of the porosity-agent particles and fibers, the space holders, so their orientation in the matrix could be implemented. For the particles, whose aspect ratios were close to 1, their orientation yielded values ranging from 11.187° to 90° (0° being perpendicular to the loading direction) for the smaller particle range, and from 20.136° to 90° for the larger particle range, which are results expected in voids generated by quasi-spheroidal particles and only slightly prolated. The front and side views of the specimens when carbamide particles (U) were used as porogens showed a regular spheroidal shape in the pore size, with no occurrence of plastic deformation in the particles provoked by the uniaxial compression (Fig. 4a-c). The sphericity of the particles (U) was confirmed using the 'inflated sphere' plugin in the reconstruction software. On the other hand, the results arising from the optimization in the fiber-void specimens (F) can be seen in Fig. 8, which shows a minimum, and therefore best fitting values, for orientations 22.79°-30.66°, and 1-2 mm fiber length, which contains the value mean aspect ratio of 9 corresponding to the average fiber length of 1.545 ± 0.651 mm.

These numerical results are in good agreement with the reconstructed data obtained from the 3D volumes by microCT and volumetric reconstruction analysis and with the predictions in Table 4 and the actual results in Table 3. Coincidentally, the side and front views of the specimens when fiber was used as space holders allowed the direct observation that fibers under consolidation preferred a perpendicular orientation to the load applied (Fig. 4d-f, 7).

The results drawn from this sub-study demonstrate that the pore aspect ratio and the pore orientation have a strong impact on the stiffness of the macrostructure.

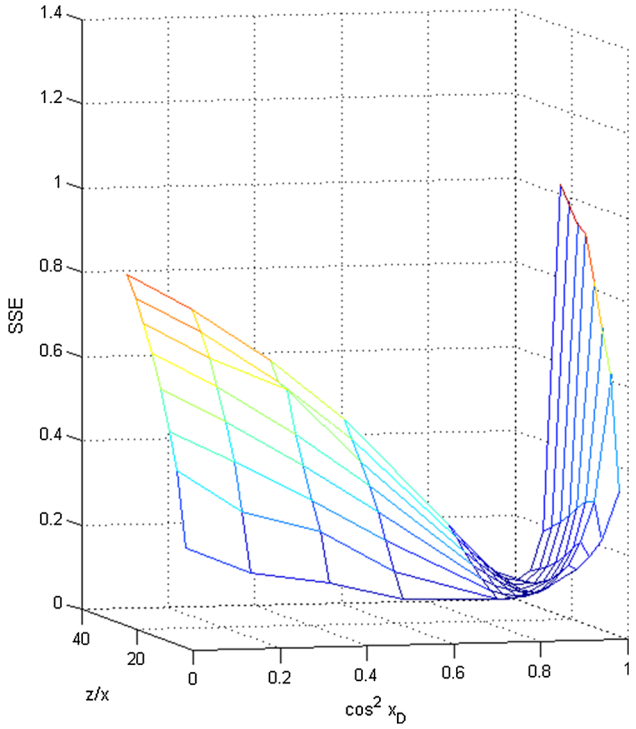

Fig. 8 Optimization method applied for the prediction of aspect ratio and orientation when fiber was used as a porogen agent, as per regression reported in Ref 20

5. Conclusions

The purpose of the study was to investigate the effect of porosity and pore morphology (size and shape) on the mechanical properties of a reportedly low corrosion, non-toxic Ti alloy (Ti35Nb4Sn) so that stiffness can be fine-tuned in the pursuit of an optimized performance, tailorable for bioengineering and lightweight structural applications. Typically reported models that predict the mechanical properties based on porosity fraction in porous materials were employed and interrogated to assess their suitability to the metal sintered porous materials fabricated 'ad-hoc' in this study. Porous specimens spanning a broad range of porosity (nominally 30-70 vol.%) were manufactured in two pore sizes ranges (a lower range 180-500 μm and a higher range 300-500 μm) and in two shapes (quasi-spheroidal and fiber-like) which were created in the sintered specimens via the use of a space holder as porogen agent and powder metallurgy. Their porosity fraction was controlled independently from pore morphology. Results from testing confirmed that porosity impacts mechanical properties (in particular stiffness) on a fashion that follows power-law models reported in the literature most faithfully and that regression to other models such as linear correlations required the use of updated coefficients for them to be better-fitting than when compared to the current library of coefficients. Results from this study confirmed that pore size has a mild impact on bulk stiffness when studied independently from porosity. On the contrary, pore shape has a significant effect on mechanical properties, with strength decreasing and residual strain increasing with higher aspect ratios of the pore geometry. It is also reported in this work that high aspect ratio pores loaded perpendicularly to the alignment direction weakened the structure when compared to spheroidal voids for equivalent volumetric porosities. Models that permit the prediction of pore morphology and orientation were successfully utilized.

These findings confirm that the hypothesis-driven design of microstructures with tailored mechanical properties is attainable through the independent definition of porosity, pore size, morphology and orientation.

Acknowledgments

The authors would like to thank Scott Doak at Loughborough Materials Characterization Centre for SEM images, Dr Patricia D Sterpaio at Abertay University for microCT scanning and support in 3D reconstruction, and Scott McFarlane for porosimetry tests.

Author's Contributions

CTS conceived the study, characterized the materials and macro/microstructures, performed numerical studies and wrote the manuscript. JMcL and RB prepared the samples and characterized the macrostructures.

Funding

This research did not receive any specific grant from funding agencies in the public, commercial or not-for-profit sectors.

References

1. J.M. Dewey, The Elastic Constants of Materials Loaded with Non-Rigid Fillers, *J. Appl. Phys.*, 1947, **18**(6), p 578–581
2. D.P.H. Hasselman and R.M. Fulrath, Effect of Small Fraction of Spherical Porosity on Elastic Moduli of Glass, *J. Am. Ceram. Soc.*, 1964, **47**(1), p 52–53
3. M.Y. Balshin, Relation of Mechanical Properties of Powder Metals and their Porosity and the Ultimate Properties of Porous Metal-Ceramic Materials, in *Dokl Akad Nauk SSSR*, 1949, pp. 831–834
4. A.K. Maitra and K.K. Phani, Ultrasonic Evaluation of Elastic Parameters of Sintered Powder Compacts, *J. Mater. Sci.*, 1994, **29**(17), p 4415–4419
5. L.J. Gibson and M.F. Ashby, *Cellular Solids: Structure and Properties*, 2nd ed., Cambridge University Press, Cambridge, 1997
6. M. Eudier, The Mechanical Properties of Sintered Low-Alloy Steels, *Powder Metall.*, 1962, **5**(9), p 278–290
7. O. Ishai and L.J. Cohen, Elastic Properties of Filled and Porous Epoxy Composites, *Int. J. Mech. Sci.*, 1967, **9**(8), p 539–546
8. R.M. Spriggs, Expression for Effect of Porosity on Elastic Modulus of Polycrystalline Refractory Materials, Particularly Aluminum Oxide, *J. Am. Ceram. Soc.*, 1961, **44**(12), p 628–629
9. F.P. Knudsen, Effect of Porosity on Young's Modulus of Alumina, *J. Am. Ceram. Soc.*, 1962, **45**(2), p 94–95

10. R.W. Rice, Extension of the Exponential Porosity Dependence of Strength and Elastic Moduli, *J. Am. Ceram. Soc.*, 1976, **59**, p 536–537
11. B. Paul, *Prediction of Elastic Constants of Multiphase Materials*. Technical Report No. 3, Brown Univ., Providence, 1959
12. D.P.H. Hasselman, On the Porosity Dependence of the Elastic Moduli of Polycrystalline Refractory Materials, *J. Am. Ceram. Soc.*, 1962, **45**(9), p 452–453
13. D.P. Mondal, N. Ramakrishnan, K.S. Suresh, and S. Das, On the Moduli of Closed-Cell Aluminum Foam, *Scrip. Mater.*, 2007, **57**(10), p 929–932
14. S. Spinner, F.P. Knudsen and L. Stone, Elastic Constant- Porosity Relations for Polycrystalline Thoria. *J. Res. Natl. Bur. Stand. C Eng. Instrum.*, 1963, Medium: X; Size: Article No. 39
15. J.K. Mackenzie, The Elastic Constants of a Solid containing Spherical Holes, *Proc. Phys. Soc. Lond. B*, 1950, **63**(1), p 2
16. L.F. Nielsen, Strength and Stiffness of Porous Materials, *J. Am. Ceram. Soc.*, 1990, **73**(9), p 2684–2689
17. T.T. Wu, The Effect of Inclusion Shape on the Elastic Moduli of a Two-Phase Material, *Int. J. Solids Struct.*, 1966, **2**(1), p 1–8
18. C.W. Bert, Prediction of Elastic Moduli of Solids with Oriented Porosity, *J. Mater. Sci.*, 1985, **20**(6), p 2220–2224
19. L. Griffiths, M.J. Heap, T. Xu, C.-F. Chen, and P. Baud, The Influence of Pore Geometry and Orientation on the Strength and Stiffness of Porous Rock, *J. Struct. Geol.*, 2017, **96**, p 149–160
20. A.R. Boccaccini, G. Ondracek et al., On the Effective Young's Modulus of Elasticity for Porous Materials: Microstructure Modelling and Comparison Between Calculated and Experimental Values, *J. Mech. Behav. Mat.*, 1993, **4**, p 119–126
21. D.S. Li, Y.P. Zhang, X. Ma, and X.P. Zhang, Space-Holder Engineered Porous NiTi Shape Memory Alloys with Improved Pore Characteristics and Mechanical Properties, *J. Alloys Compd.*, 2009, **474**(1–2), p L1–L5
22. J. Xiong, Y. Li, X. Wang, P. Hodgson, and C.E. Wen, Mechanical Properties and Bioactive Surface Modification via Alkali-Heat Treatment of a Porous Ti-18Nb-4Sn Alloy for Biomedical Applications, *Acta Biomater.*, 2008, **4**(6), p 1963–1968
23. B. Jiang, N.Q. Zhao, C.S. Shi, X.W. Du, J.J. Li, and H.C. Man, A Novel Method for Making Open Cell Aluminum Foams by Powder Sintering Process, *Mater. Lett.*, 2005, **59**(26), p 3333–3336
24. W. Niu, C. Bai, G. Qiu, and Q. Wang, Processing and Properties of Porous Titanium Using Space Holder Technique, *Mater. Sci. Eng. A*, 2009, **506**(1–2), p 148–151
25. A. Bansiddhi and D.C. Dunand, Shape-memory NiTi Foams Produced by Solid-State Replication with NaF, *Intermetallics*, 2007, **15**(12), p 1612–1622
26. Y. Torres, J.J. Pavón, and J.A. Rodríguez, Processing and Characterization of Porous Titanium for Implants by Using NaCl as Space Holder, *J. Mater. Process. Technol.*, 2012, **212**(5), p 1061–1069
27. J. Jakubowicz, G. Adamek, and M. Dewidar, Titanium Foam Made with Saccharose as a Space Holder, *J. Porous Mater.*, 2013, **20**(5), p 1137–1141
28. M. Köhl, T. Habijan, M. Bram, H.P. Buchkremer, D. Stöver, and M. Köller, Powder Metallurgical Near-Net-Shape Fabrication of Porous NiTi Shape Memory Alloys for Use as Long-Term Implants by the Combination of the Metal Injection Molding Process with the Space-Holder Technique, *Adv. Eng. Mater.*, 2009, **11**(12), p 959–968
29. M.E. Gomes, J.S. Godinho, D. Tchalamov, A.M. Cunha, and R.L. Reis, Alternative Tissue Engineering Scaffolds Based on Starch: Processing Methodologies, Morphology, Degradation and Mechanical Properties, *Mater. Sci. Eng. C*, 2002, **20**(1–2), p 19–26
30. A. Mansourighasri, N. Muhamad, and A.B. Sulong, Processing Titanium Foams Using Tapioca Starch as a Space Holder, *J. Mater. Process. Technol.*, 2012, **212**(1), p 83–89
31. Z. Esen and Ş. Bor, Processing of Titanium Foams Using Magnesium Spacer Particles, *Scrip. Mater.*, 2007, **56**(5), p 341–344
32. H. Matsumoto, S. Watanabe, and S. Hanada, Beta TiNbSn Alloys with Low Young's Modulus and High Strength, *Mater. Trans.*, 2005, **46**(5), p 1070–1078
33. Y.F. Zheng, B.L. Wang, J.G. Wang, C. Li, and L.C. Zhao, Corrosion Behaviour of Ti-Nb-Sn Shape Memory Alloys in Different Simulated Body Solutions, *Mater. Sci. Eng. A*, 2006, **438–440**, p 891–895
34. A. Nouri, P.D. Hodgson, and C. Wen, Effect of Ball-Milling Time on the Structural Characteristics of Biomedical Porous Ti-Sn-Nb Alloy, *Mater. Sci. Eng. C*, 2011, **31**(5), p 921–928
35. A. Nouri, P.D. Hodgson, and C.E. Wen, Effect of Process Control Agent on the Porous Structure and Mechanical Properties of a Biomedical Ti-Sn-Nb Alloy Produced by Powder Metallurgy, *Acta Biomater.*, 2010, **6**(4), p 1630–1639
36. R.E. Fryxell and B.A. Chandler, Creep, Strength, Expansion, and Elastic Moduli of Sintered BeO as a Function of Grain Size, Porosity, and Grain Orientation, *J. Am. Ceram. Soc.*, 1964, **47**(6), p 283–291
37. F. Gatto, Influence of Small Cavities on Velocity of Sound in Metals, *Alluminio*, 1956, **19**(1), p 19–26
38. A.S. Wagh, R.B. Poeppel, and J.P. Singh, Open Pore Description of Mechanical Properties of Ceramics, *J. Mater. Sci.*, 1991, **26**(14), p 3862–3868
39. R.B. Martin and R.R. Haynes, Confirmation of Theoretical Relation Between Stiffness and Porosity in Ceramics, *J. Am. Ceram. Soc.*, 1971, **54**(8), p 410–411
40. N. Ramakrishnan and V.S. Arunachalam, Effective Elastic Moduli of Porous Solids, *J. Mater. Sci.*, 1990, **25**(9), p 3930–3937
41. Z. Hashin, The Elastic Moduli of Heterogeneous Materials, *J. Appl. Mech.*, 1962, **29**(1), p 143–150
42. C.E. Wen, M. Mabuchi, Y. Yamada, K. Shimojima, Y. Chino, and T. Asahina, Processing of Biocompatible Porous Ti and Mg, *Scrip. Mater.*, 2001, **45**(10), p 1147–1153
43. C.E. Wen, Y. Yamada, K. Shimojima, Y. Chino, T. Asahina, and M. Mabuchi, Processing and Mechanical Properties of Autogenous Titanium Implant Materials, *J. Mater. Sci. Mater. Med.*, 2002, **13**(4), p 397–401
44. N. Tuncer, G. Arslan, E. Maire, and L. Salvo, Influence of cell aspect ratio on architecture and compressive strength of titanium foams, *Mater. Sci. Eng. A*, 2011, **528**(24), p 7368–7374
45. M. O'Neill, M.K. Haas, B.K. Peterson, R.N. Vrtis, S.J. Weigel, D. Wu, M.D. Bitner, E.J. Karwacki, Impact of Pore Size and Morphology of Porous Organosilicate Glasses on Integrated Circuit Manufacturing, MRS Proceedings 914 (2011)
46. C.T. Herakovich and S.C. Baxter, Influence of Pore Geometry on the Effective Response of Porous Media, *J. Mater. Sci.*, 1999, **34**(7), p 1595–1609